

# Direct Simulation of Low-Pressure Supersonic Gas Expansions and its Experimental Verification

Alexander Naß and Erhard Steffens

*Physikalisches Institut, Universität Erlangen-Nürnberg, 91058 Erlangen, Germany*

---

## Abstract

The use of gas expansions to generate atomic or molecular beams has become a standard technique in nuclear and hadron physics for the production of polarized ion beams and gas targets. A direct simulation Monte Carlo method was used to understand the processes occurring in an expansion of highly dissociated hydrogen or deuterium gas at low densities. The results were verified in several measurements including time-of-flight and beam-profile determinations which showed that the supersonic gas expansions can properly be described by the Monte Carlo calculations. Additionally a new method of beam formation, the hollow carrier jet, was tested under the conditions of the atomic beam source operation.

*Key words:* Monte-Carlo, Polarized Targets, Free Molecular Flows

*PACS:* 02.70.Uu, 29.25.Pj, 47.45.Dt

---

## 1 Introduction

Polarized atomic beam sources (ABS) as described, e.g., in Refs. [1] and [2] are utilized to provide nuclear-polarized atomic hydrogen (H) and deuterium (D) beams. Molecular H<sub>2</sub> or D<sub>2</sub> gas is dissociated and the essentially atomic gas then expands through a cooled nozzle into the vacuum. A beam of high brightness is then formed by a skimmer and a collimator of dimensions and positions to adapt the beam to the relatively small acceptance of the subsequent system of sextupole magnets. Based on the Stern-Gerlach principle, these magnets focus (defocus) atoms with electron-spin projection +1/2 (-1/2) along the magnetic field within the magnet bores. The electron-spin polarized beam then enters an rf transition unit, which allows to change the nuclear polarization by inducing transitions between the hyperfine states. Descriptions of the HERMES polarized ABS are given in Refs. [3] and [4]. Details about its

13.56 MHz rf dissociator are found in Ref. [5], whereas the 2.45 GHz microwave dissociator and the atomic beam test stand are described in Ref. [6].

To achieve a high output intensity, the atomic beam generated by the expansion has to fulfill several requirements like high flow rate, low transversal and longitudinal temperature, and a high degree of dissociation. The latter can only be achieved, if the recombination is low. This request sets a limit to the gas pressure in the dissociator volume of a few mbar. The pressure within and at the exit of the nozzle corresponds to the transition region between laminar and molecular flow. There, the use of continuum-flow models (e.g., those based on the Navier-Stokes equations) is of restricted validity. Thus, a direct simulation Monte-Carlo (DSMC) method [7] was used to describe the processes during gas expansion. Time-of-flight (TOF) and, with the use of a novel type of monitor [8], beam-profile measurements were performed to check the validity of the results of the simulations. The investigation of the thermal properties of the gas in the nozzle region gave new insights. The achieved results could be used to improve the beam formation and to properly determine the beam parameters. The use of an over-expanded carrier jet, surrounding the inner atomic beam, had been proposed [9] to further increase the atomic beam intensity. This method of beam formation has been studied experimentally for the first time. The results could be interpreted by DSMC calculations. A detailed description of the performed work is found in Ref. [10].

## 2 Supersonic Gas Expansion

A free-jet atomic or molecular beam can be produced by a supersonic gas expansion from a high-pressure gas source into a low pressure background. Fig. 1 shows the structure of a free expansion under continuum (steady state) conditions. The source is a short conical nozzle. As a result of the pressure difference  $p_0 - p_b$ , the gas is accelerated. At the nozzle exit the flow may reach

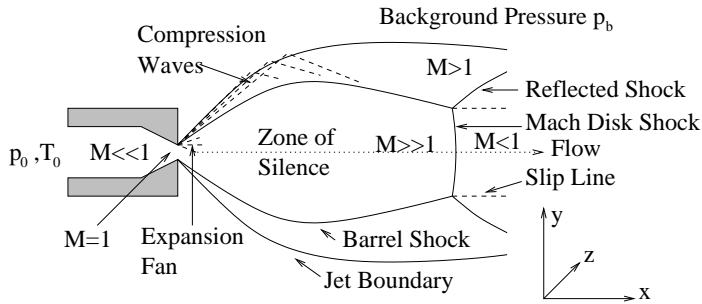


Fig. 1. Continuum free-jet expansion of a gas into a region of background pressure  $p_b$  starting from a negligibly small velocity at the stagnation state, described by  $p_0$  and  $T_0$  (figure taken from Ref. [11]).

sonic speed, if the ratio  $p_0/p_b$  exceeds the critical value [11]

$$G = \left( \frac{\gamma + 1}{2} \right)^{\gamma/(\gamma-1)}. \quad (1)$$

From the possible values of  $\gamma$ , defined as  $\gamma = c_p/c_V$  with the heat capacities  $c_p$  and  $c_V$ , it follows that for all gases  $G$  is lower than 2.05. For  $p_0/p_b < G$  the flow exits subsonically. A supersonic beam has two important characteristic properties. First, the velocity of the beam  $v$  increases during the expansion. Second, the beam parameters in the zone of silence (Fig. 1) are independent of boundary conditions (walls,  $p_b$ ), which is caused by the fact that information propagates at the speed of sound, whereas the gas moves faster. Therefore a skimmer is placed inside this zone to extract a supersonic beam. If the background pressure  $p_b$  is small enough, a smooth transition to molecular flow occurs and no shock structures emerge. The beam is only affected by residual gas scattering.

## 2.1 Thermodynamic analysis

Considering an ideal expanding gas without viscous and heat-conduction effects, the energy equation [11]

$$h + \frac{v^2}{2} = h_0 \quad (2)$$

holds, where  $h_0$  is the total or stagnation enthalpy per unit mass and  $v$  is the mean velocity in beam direction. For ideal gases ( $dh = c_p dT$ ) and constant heat capacity  $c_p = (\gamma/(\gamma - 1))(k_B/m)$  one gets the maximum or terminal velocity (for  $T \ll T_0$  after the expansion)

$$v_\infty = \sqrt{\frac{2k_B}{m} \left( \frac{\gamma}{\gamma - 1} \right) T_0}, \quad (3)$$

with the particle mass  $m$  and the Boltzmann constant  $k_B$ . For  $H_2$  ( $\gamma = 5/3$ ) at  $T_0 = 100$  K,  $v_\infty$  is 1436 m/s. For mixtures of ideal gases, an average heat capacity

$$\bar{c}_p = \frac{\sum_i k_B x_i \frac{\gamma_i}{\gamma_i - 1}}{\sum_i x_i m_i} \quad (4)$$

can be used, where  $x_i$  is the fraction of the respective species. In the continuum limit the mean velocities of the species tend to be the same [11].

For isentropic expansion of an ideal gas, eq. 2 allows to deduce

$$\frac{T}{T_0} = \left( 1 + \frac{\gamma - 1}{2} M^2 \right)^{-1} \quad (5)$$

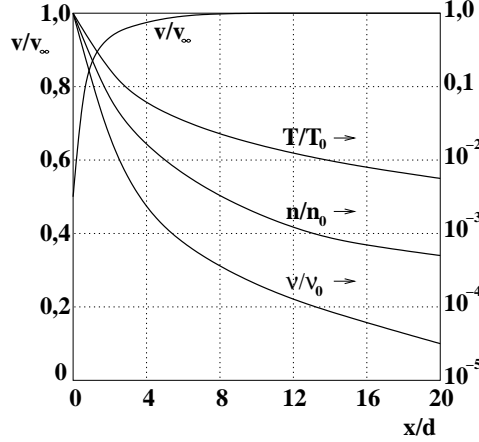


Fig. 2. Free-jet on-axis properties versus distance from the source (given in source diameters) for a monoatomic gas ( $\gamma=5/3$ ). The temperature  $T$ , the density  $n$ , and the binary hard-sphere collision frequency  $\nu$  are normalized by the source-stagnation values  $T_0$ ,  $n_0$ , and  $\nu_0$  (figure taken from Ref. [11]).

with the assumption of constant  $c_p$ . Here  $M = v/c$  is the Mach number with the speed of sound  $c = \sqrt{\gamma k_B T/m}$ . Furthermore, the mean beam velocity of the expanding gas as function of the Mach number is derived as

$$v = M \sqrt{\frac{\gamma k_B T_0}{m}} \left(1 + \frac{\gamma - 1}{2} M^2\right)^{-1/2}. \quad (6)$$

With the assumption  $M = 1$ , which is expected around the nozzle exit, for  $H_2$   $v$  is 718 m/s. In general, with the use of  $M$  as calculated [11] for axisymmetric expansion, all thermodynamic variables for the free-jet expansion can be given as shown in Fig. 2 for their dependences along the centerline of the expansion.

Energy and enthalpy considerations [12], based on Eqn. 2, for an expanding beam of a monoatomic gas ( $c_p = (5/2)(k_B/m)$ ), lead to the balance equation

$$\frac{5}{2} k_B T_0 = \frac{1}{2} m v_x^2 + \frac{3}{2} k_B T + k_B T. \quad (7)$$

In the term on the left side  $T_0$  is the stagnation temperature of the gas in the source, i.e., for thermal equilibrium the nozzle temperature  $T_{\text{nozzle}}$ . The sum of the first and second term on the right side gives the total beam energy  $E_{\text{beam}}$  after transition to molecular flow. The third term is the energy  $k_B T = pV$ , stored in the gas and forcing it to expand. For  $T_0 = T_{\text{nozzle}}$  one expects

$$\frac{3}{2} < \frac{E_{\text{beam}}}{k_B T_{\text{nozzle}}} < \frac{5}{2}. \quad (8)$$

## 2.2 Statistical definitions for the Monte Carlo method

The Monte Carlo method is another way to obtain the parameters of the atomic or molecular beam by simulating binary hard-sphere collisions between the particles of the expanding gas. The thermal velocity  $\mathbf{v}'$  of a particle of velocity  $\mathbf{v}_p$  in a beam of mean velocity  $\mathbf{v}$  is defined by

$$\mathbf{v}'_p = \mathbf{v}_p - \mathbf{v}. \quad (9)$$

The scalar pressure is defined as [7]

$$p = \frac{1}{3}nm\overline{(v'_p)^2}, \quad (10)$$

where  $n$  is the particle density,  $m$  the particle mass, and  $v'_p = |\mathbf{v}'_p|$ . With the ideal gas law  $p = nk_B T$ , the average kinetic energy associated with the translational motion becomes

$$E_{\text{tr}} = \frac{1}{2}m\overline{v'^2_p} = \frac{3}{2}k_B T_{\text{tr}}. \quad (11)$$

For every component  $j$  this can be written as

$$m\overline{v'^2_{p,j}} = k_B T_{\text{tr},j}, \quad j = x, y, z \quad (12)$$

For molecules the rotational and vibrational excitations have to be considered. They can be ascribed to an internal energy

$$E_{\text{int}} = \frac{1}{2}\zeta k_B T_{\text{int}}, \quad (13)$$

where  $\zeta$  is the number of internal degrees of freedom.

For a gas in (local) thermal equilibrium, the fraction of the particles which are found within a velocity space element  $d\mathbf{v}_p$  is given by the thermal velocity distribution [7]

$$\begin{aligned} \frac{dn}{n} &= \left(\frac{\beta}{\sqrt{\pi}}\right)^3 \exp(-\beta^2 v'^2_p) d\mathbf{v}'_p \\ &= \left(\frac{\beta}{\sqrt{\pi}}\right)^3 \exp[-\beta^2 (v'^2_{p,x} + v'^2_{p,y} + v'^2_{p,z})] dv'_{p,x} dv'_{p,y} dv'_{p,z}, \end{aligned} \quad (14)$$

where  $\beta = \sqrt{m/(2k_B T_{\text{tr}})}$ . The fraction of particles with a velocity component in  $j$  direction within the velocity range  $v'_{p,j} \dots v'_{p,j} + dv'_{p,j}$ , irrespectively of the magnitude of the other components, is obtained by integrating over the two other components. The distribution function for the thermal velocity

component then is

$$f(v'_{p,j}) = \frac{\beta_j}{\sqrt{\pi}} \exp[-\beta_j^2 v_{p,j}^2] = \frac{\beta_j}{\sqrt{\pi}} \exp[-\beta_j^2 (v_{p,j} - v_j)^2], \quad (15)$$

where  $\beta_j = \sqrt{m/(2k_B T_{tr,j})}$ . The most probable thermal velocity of each component is zero.

### 3 Simulation Program and Experimental Setup

#### 3.1 The direct simulation Monte Carlo program

The direct simulation Monte Carlo method (DSMC) [7] is a technique for the computer modeling of a real gas by some thousands or millions of simulated particle trajectories. The velocity components and position coordinates of these particles evolve in time as the particles are concurrently followed through representative collisions and boundary interactions in the physical space. The decoupling of the motion and collisions of the particles over small time steps and the division of the flow field into small cells are the key computational assumptions associated with the DSMC method. The time step should be much smaller than the mean collision time and a typical cell dimension should be much smaller than the local mean free path. The program [13] has a flexible system for the specification of the flow geometry. For our purpose the geometry of the beam forming elements nozzle, skimmer, and collimator are implemented as boundary walls with temperature  $T$  for an axially symmetric flow. Fig. 3 shows these elements together with the regions into which the flow field is divided. These regions are divided into the small cells mentioned above. Additionally, the applied input flows are indicated. The main flow is the hydrogen flow through the cooled nozzle. In addition flow losses have to be compensated. So-called Specified Flows, have to be included to simulate the chamber pressure since particles disappear which pass the outer boundaries of the regions 3 and 6. The parameters of the gas, to be calculated for every cell of these regions, are collected in the Appendix.

#### 3.2 Experimental setup and data analysis

An atomic beam test stand (ABT) had been set up [6] and equipped with several diagnostic devices (Fig. 4). It consists of a four-stage differentially pumped vacuum system with a nominal pumping speed of 14000 l/s. A dissociator mounted on the first chamber produces atomic hydrogen or deuterium.

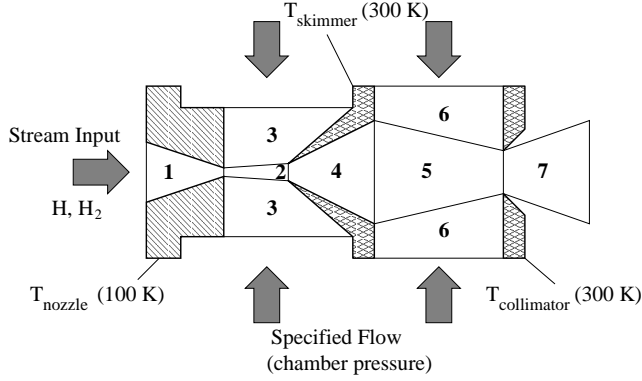


Fig. 3. The geometry employed in the simulation of an expansion in the ABS. The nozzle, skimmer, and collimator were implemented with the respective temperatures, the space in-between is divided into regions. Due to symmetry, only the upper half is calculated in the simulations. Specified Flows compensate for losses of particles at the outer boundaries of regions 3 and 6. There is no Specified Flow in region 7 to allow extraction of the beam parameters.

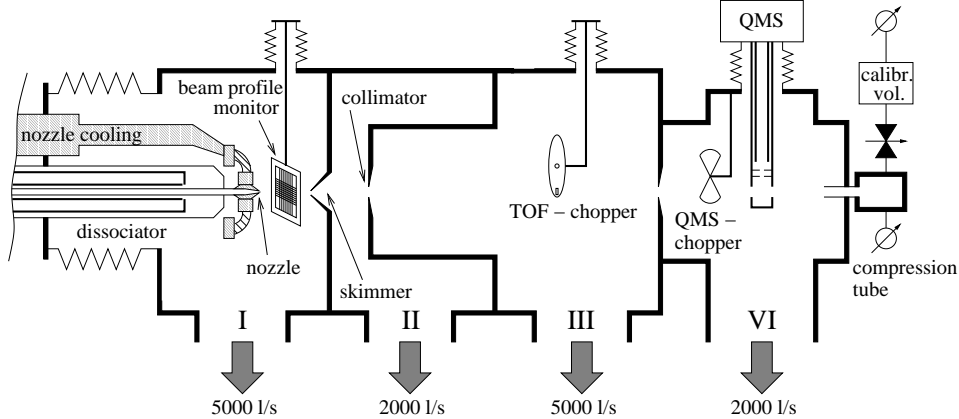


Fig. 4. The atomic beam test stand with the pumping stages I-IV. The pumping speeds are the nominal speeds for hydrogen. The signals from the quadrupole mass spectrometer are read out either with a secondary-electron multiplier or a Faraday cup.

Two types of dissociators were used: (i) a radio frequency dissociator (RFD) [5], consisting of a LC circuit as a field applicator and a water cooled Pyrex discharge tube, and (ii) a microwave dissociator (MWD) [6], based on a plasma source which couples a 2.45 GHz surface wave to the discharge in an air-cooled Pyrex glass tube. The H (D) gas expands through a nozzle, cooled by a 120 W closed-cycle helium cold head. Together with a skimmer and a collimator a high-brightness beam is formed. This beam is analyzed by means of several devices. A calibrated compression tube is used to perform absolute measurements of the beam intensity. The degree of dissociation could be determined with the quadrupole mass spectrometer (QMS). A chopper, combined with a lock-in amplifier, was used to separate the beam signal from the residual gas

background. The intensity-related degree of dissociation  $\alpha$ , defined as

$$\alpha = \frac{S_a^*}{S_a^* + 2 \kappa_{\text{ion}} \kappa_{\text{det}} \kappa_v S_m}, \quad (16)$$

was determined from the QMS signals  $S_a$  and  $S_m$  for atoms and molecules, respectively. In this equation  $S_a^* = S_a - \delta^{\text{diss}} S_m$  is the atomic signal corrected for dissociative ionization in the QMS with  $\delta^{\text{diss}} = 0.0125$  (0.0085) for hydrogen (deuterium) [6]. Furthermore,  $\kappa_{\text{ion}} = \sigma_a^{\text{ion}} / \sigma_m^{\text{ion}} = 0.64 \pm 0.04$  [14] is the ratio of the ionization cross sections and  $\kappa_{\text{det}} = w_a^{\text{det}} / w_m^{\text{det}}$  is the ratio of the detection probabilities of the QMS either with the secondary-electron multiplier (SEM) or with the Faraday cup (FC). Since one can assume  $w_a^{\text{FC}} = w_m^{\text{FC}}$  and therefore  $\kappa_{\text{FC}} = 1$ ,  $\kappa_{\text{SEM}}$  can be determined from the ratio

$$\kappa_{\text{SEM}} = \frac{(S_a^*/S_m)_{\text{SEM}}}{(S_a^*/S_m)_{\text{FC}}}. \quad (17)$$

by measuring alternately the atomic and molecular QMS signals with the Faraday cup and the secondary-electron multiplier. With an accuracy of about 1 %,  $\kappa_{\text{SEM}}$  was determined as 0.78 ... 0.91 depending on the voltage, applied to the SEM. Finally,  $\kappa_v = v_a/v_m$  regards for the different dwell times of the atoms and molecules in the ionization volume of the QMS.

### 3.2.1 Velocity analysis

The velocity distribution of the particles in the atomic beam is determined with the time-of-flight (TOF) method. A fast chopper cuts a small bunch of particles out of the beam, and their arrival time at the QMS is measured. Since the particles have different velocities, a TOF distribution  $F(t)$  is measured. To keep the influence of the opening function of the chopper small, the rotational frequency of the motor had to be high and stable. For this reason a special stepping motor was used, installed in chamber III of the setup (Fig. 4). A light-barrier signal defined the zero point of the TOF distribution and triggered the oscilloscope used to store the QMS signals  $S(t)$ .

The relation between the measured TOF distribution  $F(t)$  and the velocity distribution  $f(v)$  of Eq. 15 with  $v = l_{\text{cq}}/t$  is

$$F(t) \propto \frac{1}{t^2} f\left(\frac{l_{\text{cq}}}{t}\right), \quad (18)$$

where  $l_{\text{cq}}$  is the distance between chopper and QMS. The measured signal distribution, corrected for an offset  $p_0^*$ , results from the convolution of the TOF function  $F(t)$ , the opening function of the chopper wheel  $A(t)$ , and the



response function of the electronics  $K(t)$  as

$$S(t) - p_0^* = \int_0^t K(t - \lambda) \int_0^\lambda F(\lambda - \psi) A(\psi) d\psi d\lambda. \quad (19)$$

The opening function  $A(t)$  was measured at a low rotational frequency of the chopper wheel. At 300 Hz, used in the experiments, for the slit width of 2 mm and the tangential slit velocity of 75 m/s, a good approximation is the half period of  $A(t) = A_0 \sin(\pi t/T)$  with  $A_0 = 0.278$  and  $T = 0.055 \pm 0.004$  ms. In the response function of the electronics,  $K(t) = (1/\tau_e) \exp(-t/\tau_e)$ ,  $\tau_e = 0.21 \pm 0.01$  ms is calculated from the input resistance of the oscilloscope and the cable capacity.

The measured signal distributions were fitted by functions

$$S(t) = p_0^* + \frac{p_1^*}{t^2} \exp \left\{ -\frac{m}{2k_B p_2^*} \left( \frac{l_{\text{cqi}}}{t} - p_3^* \right)^2 \right\}. \quad (20)$$

The functions  $S(t) - p_0^*$  then were de-convoluted, following the method of Ref. [15], by calculating

$$F(t_n) = \frac{\pi}{T} \sum_{i=0}^{\infty} (-1)^i \left[ S(\lambda) + \tau_e \frac{dS(\lambda)}{d\lambda} \right]_{\lambda=t_n-iT} + \frac{T}{\pi} \sum_{i=0}^{\infty} (-1)^i \left[ \frac{d^2 S(\lambda)}{d\lambda^2} + \tau_e \frac{d^3 S(\lambda)}{d\lambda^3} \right]_{\lambda=t_n-iT} \quad (21)$$

for an appropriate sequence of times  $t_n$ , covering the time range of the TOF measurement. The obtained distributions  $F(t_n)$  then were fitted by the TOF functions

$$F(t) = \frac{p_1}{t^2} \exp \left\{ -\frac{m}{2k_B p_2} \left( \frac{l_{\text{cqi}}}{t} - p_3 \right)^2 \right\}. \quad (22)$$

The fits yield  $p_1$  as a scaling factor,  $p_2$  according to Eqn. 15 yields the translational beam temperature  $T_{\text{tr},x}$ , and  $p_3$  is equal to the mean velocity  $v_x$  in beam direction, i.e., the beam parameters to be determined. Fig. 5 as an example shows a measured signal distribution and the derived TOF function.

### 3.2.2 Beam-profile monitor

A beam-profile monitor [8] was used to measure intensity profiles of the atomic hydrogen or deuterium beam. A frame, carrying 32 gold-plated tungsten wires of diameter  $d_w = 5 \mu\text{m}$  (16 wires each in horizontal and vertical direction) was placed between nozzle and skimmer. At a wire spacing of 2 mm, the wires covered the full cross section of the beam. Beam atoms, which hit a wire, get stucked at the gold cover with a probability  $w_s^{\text{Au}} = 0.5 \pm 0.1$  [16], i.e., they are

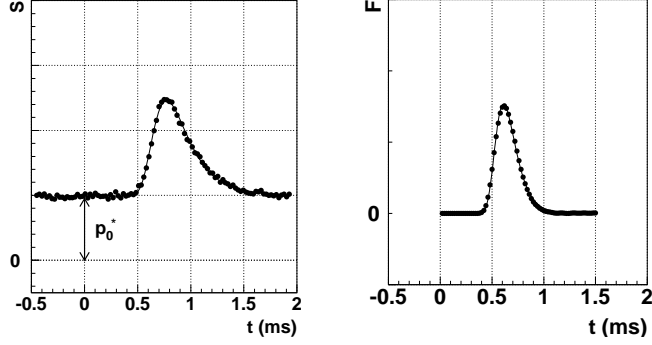


Fig. 5. Example of the measured signal distributions with the offset  $p_0^*$  and the fitted function  $S(t) - p_0^*$  of Eqn. 20 (left-hand side) and the TOF distribution  $F(t)$  (right-hand side), resulting from deconvolution, with the fitted function of Eqn. 22.

not immediately re-emitted. If stuck, the atoms recombine with atoms of the surface-covering atomic layer to form molecules, which then are emitted due to their much lower binding energy. The recombination probability  $w_r$  of stuck atoms thus can be assumed as 1.0. The recombination energy  $E_r = 4.476$  eV per  $H_2$  molecule [17] leads to a local heating and a differential increase  $dR$  of the wire resistance. For a wire of length  $L$  extending in  $z$  direction,  $dR/dz$  is a function  $f(dP/dz)$  of the differential energy deposition  $dP/dz$ . The total wire resistance is

$$R = R_0 + \int_0^L (dR/dz) dz = R_0 + \int_0^L f(dP/dz) dz, \quad (23)$$

where  $R_0$  is the wire resistance without beam. It can be assumed that (i) the wires are homogeneous along their length and that (ii) the locally produced heat is spread by radiation cooling only, i.e., that the heat transfer along the wire can be neglected. Under these assumptions, the function  $f$  can be determined for each wire by application of a series of currents  $I$  and measurement of the voltages  $U$ . Here one has  $P = U \cdot I$ ,  $dP/dz = \text{const} = P/L$ , and

$$R = R_0 + \int_0^L f(P/L) dz = R_0 + L \cdot f(P/L). \quad (24)$$

The measured response functions  $R_i(P)$  for the 32 wires are shown in Fig. 6. With some scattering, all the curves show the same behavior, an approximately linear increase from  $R_{i,0}$  at  $P = 0$  and a saturation towards higher  $P$  values caused by the increase of radiation cooling due to the increasing wire temperature.

The monitor wires are positioned at different perpendicular distances  $y_i$  from the atomic beam axis. The changes of the total wire resistances depend on the total flux of atoms, hitting the wires. Thus, on the one hand the measurement of the set of  $R_i - R_{i,0}$  yields data on the intensity distribution of the beam and

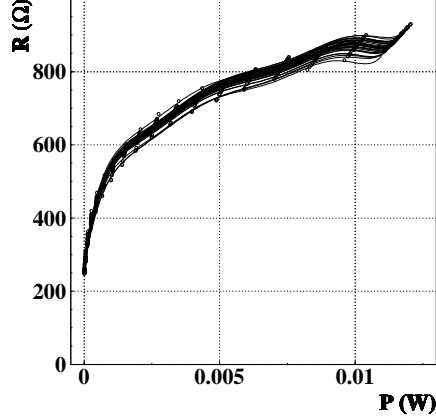


Fig. 6. The response functions of the 32 wires of the beam-profile monitor, measured by loading the wires with sequences of currents and measuring the voltages.

its development with the distance  $x$  from the nozzle exit. On the other hand, the measured data can be compared with those, which result from the DSMC calculations. These yield atomic density and velocity distributions,  $n(x, y, z)$  and  $v(x, y, z)$ , which can be used to calculate the differential recombination-energy deposition in the wires as

$$dP_i(x, y, z) = d_w \cdot w_s^{\text{Au}} \cdot w_r \cdot E_r \cdot \frac{1}{2} n(x, y, z) \cdot v(x, y, z) dz. \quad (25)$$

With the use of Eq. 25 and the measured response function  $f_i(dP/dz) = f_i(P/L)$  by summation over the wire length the increase of the wire resistance can be calculated and compared with the measured values to check the validity of the calculations.

## 4 Simulation Results and Experimental Verification

### 4.1 Molecular hydrogen beam from a cooled nozzle

First of all, a Monte Carlo simulation of an expansion of molecular hydrogen was performed. The geometry was chosen as shown in Fig. 3, the dimensions of the setup are given in Fig. 7. The parameters for the stream input were the gas temperature  $T_{\text{gas}} = 300$  K and the particle density  $n_0$  which was determined from the measured pressure  $p_0$  in front of the nozzle. The calculated flow rates through the nozzle,  $Q$ , were in good agreement with the measured primary gas flow. The parameters for the Specified Flows at the outer boundaries (Fig. 3) were obtained from the residual gas pressures  $p_b$  measured at the atomic beam-test stand at the respective flow rate  $Q$ . The calculated particle-density distribution of the entire simulated space is shown in Fig. 7. The density near the nozzle follows a  $\cos(\theta)$  distribution. Skimmer and collimator

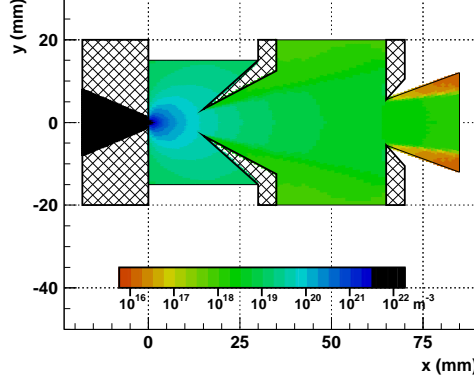


Fig. 7. The calculated particle-density distribution of a molecular hydrogen beam, expanding in the system of nozzle, skimmer, and collimator (diameters: nozzle throat 2.0 mm, skimmer top 6.4 mm, collimator 11 mm; distances: nozzle to skimmer-top 15 mm, skimmer-top to collimator 50 mm;  $T_{\text{nozzle}}$  100 K; primary molecular gas flow 1 mbar/l/s).

form a low-diverging and sharp-bound molecular beam. The density at the beam edge decreases by two orders of magnitude over a distance of 1 mm at a beam diameter of about 15 mm.

Fig. 8 shows the calculated on-axis beam properties. Within the nozzle ( $x =$

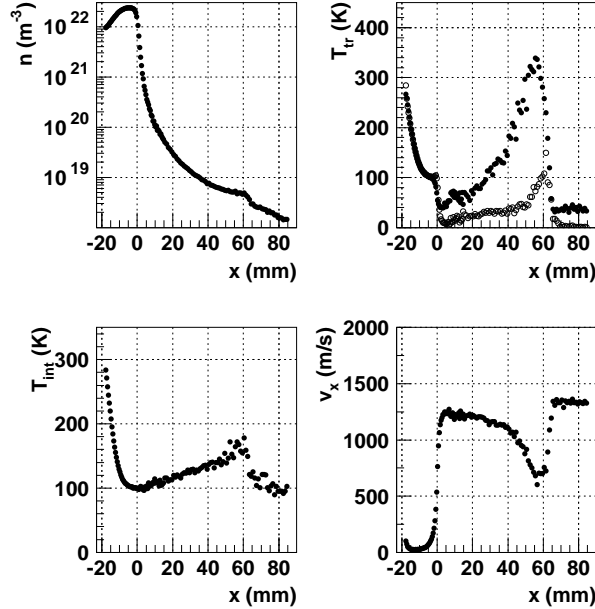


Fig. 8. On-axis beam properties, calculated for a  $\text{H}_2$  beam in the setup of Fig. 7 as function of the distance to the nozzle exit ( $n$ : particle density;  $T_{\text{tr}}$ : translational temperatures describing the velocity distributions in  $x$  (full circles),  $y$  and  $z$  direction (open circles);  $T_{\text{int}}$ : rotational temperature;  $v_x$ : mean particle velocity in  $x$  direction (along the beam axis)). The pronounced variations of  $T_{\text{tr}}$ ,  $T_{\text{int}}$ , and  $v_x$  between  $x = 2$  mm and  $x = 65$  mm are caused by the sampling of the DSMC computer code as discussed in the text.

–15 mm to 0 mm),  $T_{\text{tr}}$  and  $T_{\text{int}}$  drop to the temperature of the nozzle, i.e., the gas is thermalized, the particle density  $n$  rises, and the mean velocity  $v_x$  is low. At the exit of the nozzle (or shortly before) the expansion into the low-pressure region starts. The particle density decreases with increasing distance from the nozzle.

The increase and drop of  $T_{\text{tr}}$  and  $T_{\text{int}}$  as well as the drop and rise of  $v_x$  between  $x = 2$  mm and  $x = 65$  mm, the position of the collimator, are due to the sampling by the DSMC computer code. Every data point of the distributions of Fig. 8 results from averaging over the molecules in the entire cell. It includes beam molecules as well as residual gas molecules that will not pass the collimator. Genuine beam parameters can only be extracted from the cells with  $x > 65$  mm, since no Specified Flow is applied to region 7 (Fig. 3). Regarding this fact, one can state that for  $x > 2$  mm  $T_{\text{tr}}$ ,  $T_{\text{int}}$ , and  $v_x$  essentially stay unaffected. The reason is that the collision rate is too low to enable thermal equilibrium between translational and internal energy, which requests about 100 bounces per molecule. The internal (rotational) temperature “gets frozen” in the region of the nozzle exit. Contrary to  $T_{\text{int}}$ ,  $T_{\text{tr}}$  shows a pronounced decrease between  $x = 0$ , the nozzle exit, and  $x \sim 2$  mm, the position of the “freezing surface”. A few bounces only are required to thermalize the translational degrees of freedom. In the same  $x$  interval, the mean velocity in beam direction,  $v_x$ , increases with the decreasing translational beam temperature. Thermal energy is converted into directional motion. The temperatures  $T_{\text{tr}}$  in  $y$  and  $z$  directions are lower than that in  $x$  direction, because particles with higher transversal velocity leave the beam center, and thus the temperature on the axis drops. This effect may be denoted as “geometrical cooling”.

In the upper part of Tab. 1, the values for the mean velocity  $v_x$  and the translation temperature  $T_{\text{tr},x}$  are compared as they result from measurement and DSMC calculation, both performed under the boundary conditions given in Fig. 7. The calculated mean velocity is close to the measured one, but the resulting temperature is appreciably too high. The problem was studied [18,19] and it was found that the temperature contrary to the mean velocity, strongly depends on the parameters of the collision processes used in the simulation code. It seems that certain parameters, chosen by the editors of the simulation code [13], are not fully correct for the low-temperature region. Furthermore, the influence of background gas in the nozzle-skimmer region over the beam properties was investigated [18,19]. It could be shown that by the modification of parameters, essentially of scattering cross sections, the beam temperature can be adopted to the measured one, while the mean velocity stays almost unaffected (Tab. 1).

Table 1

Comparison of the calculated and measured parameters of (i) a pure molecular and (ii) a partly dissociated hydrogen beam. The errors of the measurements are statistical and systematical, resulting from those in the determination of  $T$  and  $\tau_e$  (section 3.2.1), respectively. The asymmetric systematical errors of the simulation results originate from discrepancies of the simulation distribution and the Maxwellian distribution used for the analysis of the experimental data [20]. The boundary conditions are given in Fig. 7. The measured mean velocity in beam direction,  $v_x$ , and the temperature  $T_{tr,x}$  result from fits according to Eqn. 22.  $M_x = v_x/\sqrt{\gamma k_B T_{tr,x}/m}$  is the axial Mach number and  $v_\infty$  is the maximum beam velocity according to Eqn. 3. The simulation calculation of Refs. [18,19] were initiated by the discrepancy encountered with the original parameters. The degree of dissociation (Eqn. 16) of the partly dissociated beam was  $\alpha = 0.63$ .

	$v_x$ (m/s)	$T_{tr,x}$ (K)	$M_x$	$v_\infty$ (m/s)
<b>molecular beam</b>				
measurement	$1274 \pm 8 \pm 13$	$19.0 \pm 1.1 \pm 0.9$	3.52	
simulation (original)	$1334 \pm 12 \begin{smallmatrix} +5 \\ -15 \end{smallmatrix}$	$33.3 \pm 1.6 \begin{smallmatrix} +0 \\ -3 \end{smallmatrix}$	2.79	1436
simulation (Refs. [18,19])	$1371 \pm 2 \begin{smallmatrix} +5 \\ -15 \end{smallmatrix}$	$19.0 \pm 0.2 \begin{smallmatrix} +0 \\ -3 \end{smallmatrix}$	3.79	1436
<b>partly dissociated beam</b>				
<b>atoms</b>				
measurement	$1750 \pm 47 \pm 24$	$25.7 \pm 4.9 \pm 1.5$	2.94	
simulation	$1760 \pm 20 \begin{smallmatrix} +6 \\ -19 \end{smallmatrix}$	$41.0 \pm 3.4 \begin{smallmatrix} +0 \\ -3 \end{smallmatrix}$	2.34	2031
<b>molecules</b>				
measurement	$1579 \pm 51 \pm 17$	$23.7 \pm 7.1 \pm 1.0$	3.91	
simulation	$1590 \pm 33 \begin{smallmatrix} +6 \\ -17 \end{smallmatrix}$	$44.0 \pm 4.3 \begin{smallmatrix} +0 \\ -3 \end{smallmatrix}$	2.89	1436

#### 4.2 Partly dissociated beam from a nozzle

With the use of the QMS, the TOF distributions of the atoms and molecules in a partly dissociated hydrogen beam were measured. The measurement was performed with the same setup of nozzle, skimmer, and collimator which was used with the pure molecular hydrogen beam. The dimensions were those given in Fig. 7. The degree of dissociation  $\alpha$ , entering the following calculations, was between 0.50 and 0.80 depending on the experimental conditions. TOF distributions were measured with nozzle temperatures  $T_{nozzle} = 70, 100, 150,$  and  $200$  K and primary molecular flows  $Q$  between  $0.5$  and  $6.9$  mbarl/s. The mean velocity and beam temperature for the atomic and the molecular fraction of the beam, measured with  $T_{nozzle} = 100$  K,  $Q = 1$  mbarl/s and  $\alpha = 0.63$  and

resulting from the fits according to Eqn. 22, together with the Mach numbers are given in the lower part of Tab. 1.

The temperature of the gas in the plasma of the microwave dissociator [6], used in these measurements, may reach values of  $T_{\text{plasma}} = 2000$  K [21] or even higher. Since the plasma end is near to the nozzle entrance, one has to investigate, whether the gas reaches thermal equilibrium in the nozzle before the expansion. According to Eqn. 8, the beam energy (in units of  $k_{\text{B}}T_{\text{nozzle}}$ ) is expected to lie in the range 3/2 to 5/2 for full temperature equilibrium of the gas in the nozzle. The left-hand part of Fig. 9 shows four sets of beam energies, calculated from  $v_x$  and  $T_{\text{tr},x}$  of both species H and H<sub>2</sub>, as function of the primary molecular flow  $Q$ .

For  $Q \leq 1$  mbarl/s, the beam energies lie in the expected range 3/2 to 5/2. For higher input flows, however, it is higher than expected. The discrepancy increases with decreasing nozzle temperature  $T_{\text{nozzle}}$  and increasing gas flow  $Q$ . This finding would be explained by the assumption that the temperature of the gas in the nozzle,  $T_0$ , is higher than  $T_{\text{nozzle}}$ , i.e., that the gas does not reach the thermal equilibrium. For  $Q = 1$  mbarl/s and  $T_{\text{nozzle}}$ , this explanation was studied by DSMC calculations. The right-hand part of Fig. 9 shows the calculated on-axis temperature of the gas in the nozzle cone ( $T_{\text{nozzle}} = 100$  K) as a function of distance to the nozzle exit for four temperatures  $T_{\text{Plasma}}$  of the gas entering the nozzle. For  $T_{\text{Plasma}} = 300$  K, the thermalization is complete, while for higher  $T_{\text{Plasma}}$  the thermalization is incomplete,  $T_0 > T_{\text{nozzle}}$ , and hence the beam energy exceeds  $5/2 k_{\text{B}}T_{\text{nozzle}}$ . Because the exact gas temperature in the plasma is not known, in the further DSMC calculations  $T_{\text{plasma}} = 3000$  K was used as the temperature of the gas, entering the nozzle.

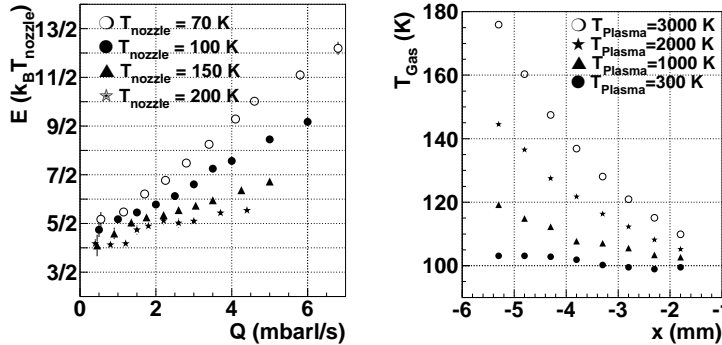


Fig. 9. Left-hand side: beam energies, as defined in Eqn. 7 and calculated from the measured velocity distributions of H and H<sub>2</sub>, as function of the primary molecular gas flow  $Q$ . Each of the four sets is given in units of  $k_{\text{B}}T_{\text{nozzle}}$  with the respective nozzle temperature. Right-hand side: on-axis gas-temperature distributions in the nozzle ( $T_{\text{nozzle}} = 100$  K), calculated with the DSMC code for  $Q = 1$  mbarl/s,  $\alpha = 0.67$  and four temperatures of the plasma in the microwave dissociator, as function of the distance to the nozzle exit.

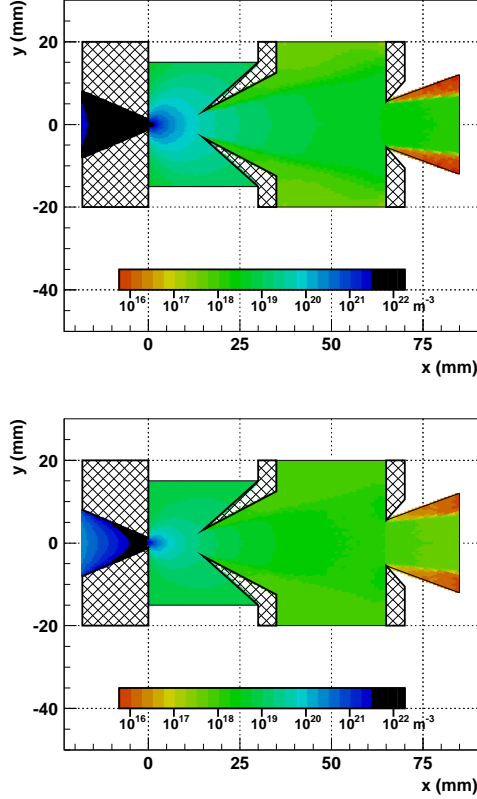


Fig. 10. The calculated density distribution of the atomic (upper plot) and molecular (lower plot) fraction of a partly dissociated hydrogen beam ( $\alpha = 0.63$ ) for  $T_{\text{nozzle}} = 100$  K and  $Q = 1$  mbar $l/s$ .

The calculated density distribution of the atomic and molecular fraction are shown in Fig. 10. As for the pure molecular beam, low-diverging atomic and molecular beams with sharp boundaries are obtained, formed by skimmer and collimator. The distributions of the on-axis beam properties (particle density, translational and internal temperature, and mean velocity) are similar to those shown in Fig. 8 for the pure molecular beam. The calculated mean velocities and temperatures for the atomic and molecular fraction in Tab. 1 are juxtaposed with the measured values. Both the measured and calculated values of the mean molecular velocity are in good agreement. They show that in the expansion of a gas mixture the heavier species (molecules) are accelerated above the theoretical limit of a pure expansion, which would yield  $v_{x,H_2} = v_{x,H}/\sqrt{2}$ . As for the pure molecular beam, one finds a deviation of the simulated from the measured temperatures, while the mean velocities agree. The reason for this difference is the same as discussed for the DSMC calculations for the molecular beam.



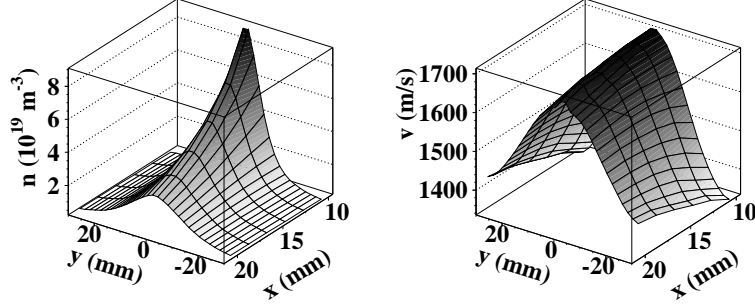


Fig. 11. Calculated distributions of the atomic hydrogen density  $n(x, y, z = 0)$  (left-hand histogram) and of the mean velocity of the atoms  $v(x, y, z = 0)$  (right-hand histogram). The data of the atomic beam stem from a DSMC calculation of the expansion of a partly dissociated hydrogen beam (rf dissociator with plasma temperature  $T_{\text{plasma}} = 3000$  K, degree of dissociation  $\alpha = 0.76$ ), and nozzle temperature  $T_{\text{nozzle}} = 100$  K. Because of cylindrical symmetry the dependence on  $z$  at  $y = 0$  is identical to the  $y$  dependence at  $z = 0$  shown.

### 4.3 Beam profiles

The data, obtained by the DSMC calculations for a partly dissociated hydrogen beam, could be further compared with the results of beam-profile measurements, made with the beam-profile monitor described in the section 3.2.2. The distance between nozzle and skimmer had to be increased from 15 mm (Fig. 7) to 50 mm to allow positioning and moving of the monitor in-between along the beam axis. Therefore, only the expansion from the nozzle exit into the low-pressure region between nozzle and skimmer was considered. The input geometry of the DSMC code was reduced to this region and the skimmer was assumed to be the transition to vacuum. The calculated density distribution  $n(x, y, z)$  and velocity distribution  $v(x, y, z) = \sqrt{v_x^2(x, y, z) + v_y^2(x, y, z) + v_z^2(x, y, z)}$  are shown in Fig. 11. The left-hand histogram indicates, how the total density of particles decreases from the beam axis ( $y = 0$ ) to zero. Contrary to that, the mean velocity of the atoms, shown in the right-hand histogram, decreases only slightly from the on-axis value of about 1700 m/s, comparable to those of Tab. 1, to about 1400 m/s. In the covered range of  $x$ , the density shows a distinct decrease, whereas the velocity stays more or less unchanged due to the fact that already the minimum  $x$  position of 10 mm is far behind that of the freezing surface at about 2 mm.

The beam monitor allows to measure the change of the resistance of each of the wires by surface recombination of the hydrogen atoms in the beam (cf. section 3.2.2). In the used coordinate system, given in Fig. 1, each of the wires extends along the  $z$  direction with a perpendicular distance  $y$  to the beam axis in a plane, positioned perpendicular to the beam axis at distance  $x$  from the nozzle exit. With the calculated  $n(x, y, z)$  and  $v(x, y, z)$ , the differential heat deposition in a wire can be calculated with the use of Eqn. 25. Taking into

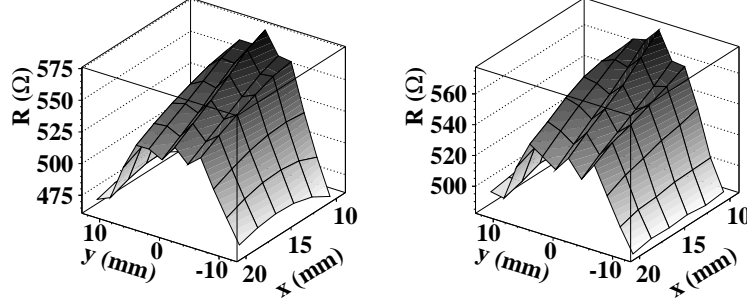


Fig. 12. Calculated (left-hand part) and measured (right-hand part) distribution of the wire resistances (the geometry and the experimental parameters are those given in Figs. 10 and 11).

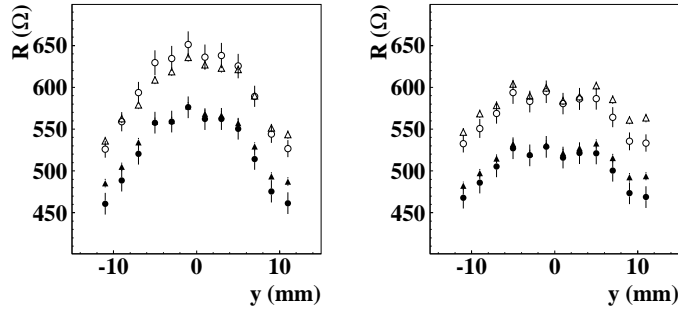


Fig. 13. Comparison of the calculated (circles) and measured (triangles) distributions of the wire resistances at distances between wire plane and nozzle exit of 10 mm (left-hand side) and 20 mm (right-hand side). The lower-lying distributions (full symbols) were obtained for the geometry and the experimental parameters given in Figs. 10 and 11, whereas the higher-lying distributions result with a primary molecular flow  $Q$  enlarged from 1 mbar/l/s to 2 mbar/l/s.

account the measured response functions of Fig. 6 and summation over the wire length yields the distribution  $R(x, y)$ . The density of the hydrogen atoms at the wire ends,  $n(y = \pm 25 \text{ mm})$ , is very small compared to that of the beam axis. Thus recombination effects on the frame could be neglected. In Fig. 12, the calculated distribution of the resistances is compared with the measured one. Both distributions are not smooth due to the variations in the response functions of the wires. Good agreement, however, is found for the shape of the distributions and their absolute values. In more detail, this is demonstrated in Fig. 13. There distributions are shown for two distances between wire plane and nozzle exit,  $x = 10 \text{ mm}$  (left-hand part) and  $x = 20 \text{ mm}$  (right-hand part). The lower-lying distributions result for the geometry of Fig. 10 and the experimental parameters of Fig. 11, i.e., they are cuts through the distributions of Fig. 12 at  $x = 10 \text{ mm}$  and  $20 \text{ mm}$ , whereas the higher-lying distributions are found for an increased primary molecular flow  $Q = 2 \text{ mbar/l/s}$ . The good agreement confirms the validity of the DSMC calculations.

#### 4.4 Hollow carrier jet

The carrier jet method was proposed [9] to increase the phase-space density of the atomic beam and thus to reach a higher intensity through the collimator of the atomic beam source. An over-expanded carrier jet, surrounding the inner atomic beam, was predicted to cool and to confine the inner beam (Fig. 14). The mixing of the two gases has to be small and the carrier gas has to be removed by the skimmer and pumped away. The present measurements and calculations were extended to investigate for the first time the idea of the carrier jet. A variety of inner/outer gas combinations were studied, namely H/H<sub>2</sub>, D/D<sub>2</sub>, D<sub>2</sub>/H<sub>2</sub>, D/He, and Ar/N<sub>2</sub>. The test stand (Fig. 4) had to be modified by replacing the turbo-molecular pumps of the first chamber by a roots-pump system with a nominal pumping speed of 1000 l/s to master the requested [9] high carrier-gas flows (up to 40 mbarl/s). The aluminum carrier-jet nozzle combines a conical inner nozzle with an outer, ring-like Laval-type nozzle to create an outer hollow beam surrounding an inner nozzle beam (Fig. 14).

##### 4.4.1 Low-mass gases

Starting with molecular deuterium D<sub>2</sub> as inner gas and molecular hydrogen H<sub>2</sub> as carrier gas, measurements were performed for a wide range of input parameters. The nozzle-throat diameter was 2 mm and the distance between the nozzle exit and the skimmer was 30 mm. The nozzle temperature was kept at  $T_{\text{nozzle}} = 100$  K. For three values of the inner D<sub>2</sub> flow of 1, 4, and 7 mbarl/s, the outer H<sub>2</sub> flow was varied from 0 up to 30 mbarl/s to approach the suggested ratio [9] of about 40. The QMS signals, which give the particle density in the ionization volume, were multiplied by the mean velocity, determined by TOF measurements, to yield the on-axis intensities. The results are presented in Fig. 15. As the left-hand part of the figure shows, no increase of the on-axis D<sub>2</sub> beam intensity is found. On the contrary, especially the intensity shows a strong decrease at 1 mbarl/s primary D<sub>2</sub> flow. The results of Fig. 15 were confirmed in further measurements with different dimensions of the outer nozzle, with different nozzle-to-skimmer distances, and with H/H<sub>2</sub>, D/D<sub>2</sub>, and

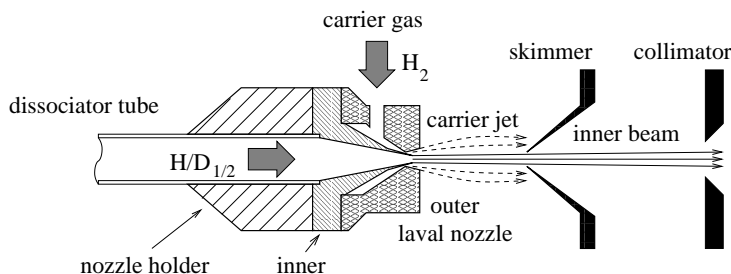


Fig. 14. The nozzle and the principle of the hollow carrier jet.

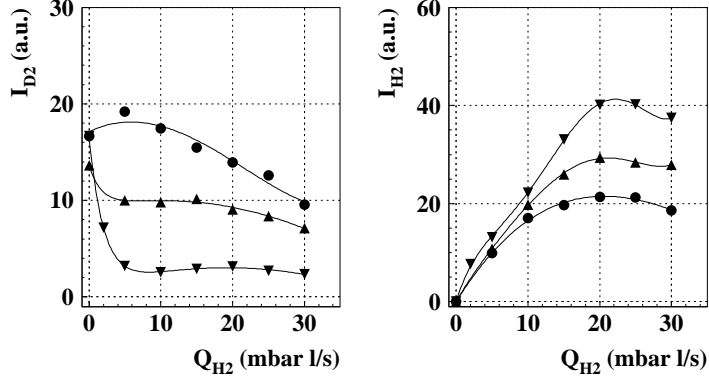


Fig. 15. Measured on-axis intensities of the inner gas  $D_2$  (left-hand side) and the carrier gas  $H_2$  (right-hand side) as a function of the primary carrier gas flow  $Q_{H_2}$  for primary inner gas flows  $Q_{D_2} = 1$  mbar/l/s (triangles down), 4 mbar/l/s (triangles up), and 7 mbar/l/s (dots). The intensities  $I_{D_2}$  and  $I_{H_2}$  are given in arbitrary, but identical, units and, thus, the given values can be compared directly.

D/He as inner/outer gases. The measured high on-axis intensities of the carrier gases indicate a pronounced mixing of the outer gas into the inner beam. This is obvious, too, from the beam parameters, mean velocity and temperature, measured for the (inner)  $D_2$  beam as shown in Fig. 16. The gas of the inner beam gets more and more accelerated with increasing carrier-jet flow. No cooling effect on the inner beam was measured.

Because of the pronounced discrepancy between the measured data and the prediction [9], the DSMC program was used to understand the mechanisms involved. The calculations were performed for a nozzle-throat diameter of 2 mm, equal to that used in the measurements, and a slightly increased distance between nozzle exit and skimmer top of 35 mm. The obtained density distributions are shown in Fig. 17. There, the upper plot shows that of the  $D_2$  beam of gas flow  $Q_{D_2} = 7$  mbar/l/s, expanding without carrier gas. The central plot presents the distribution of the  $D_2$  fraction ( $Q_{D_2} = 7$  mbar/l/s from

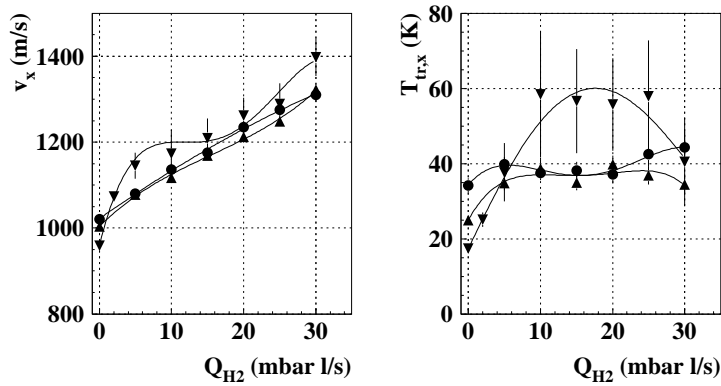


Fig. 16. Mean velocity  $v_x$  and beam temperature  $T_{tr,x}$  of the inner gas  $D_2$  as a function of the primary carrier gas flow  $Q_{H_2}$  for primary inner gas flows  $Q_{D_2} = 1$  mbar/l/s (triangles down), 4 mbar/l/s (triangles up), and 7 mbar/l/s (circles).

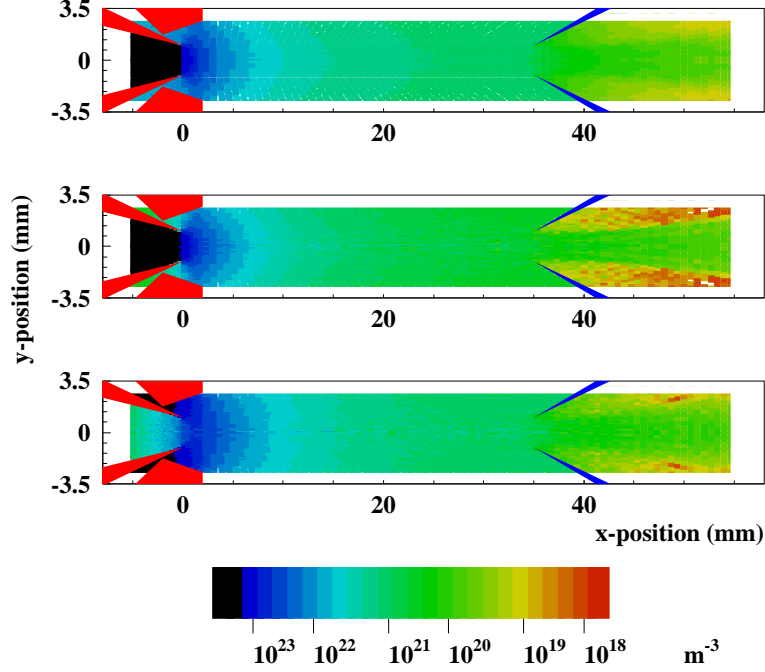


Fig. 17. Calculated distributions of the density in the expansion of an inner  $D_2$  beam without carrier jet (upper plot) and the densities of the inner,  $D_2$ , fraction (central plot) and the outer,  $H_2$ , fraction (lower plot) in the expansion with a carrier-jet. The gas flows were chosen as  $Q_{D_2} = 7$  mbarl/s and  $Q_{H_2} = 21$  mbarl/s.

the inner nozzle as in the upper plot) in the expansion with an  $H_2$  carrier jet ( $Q_{H_2} = 21$  mbarl/s) from the outer ring-shaped nozzle. The lower plot shows the density distribution of the  $H_2$  carrier molecules. No significant difference is found between the distributions in the upper and central plot. In agreement with the measurements, the comparison of the central and the lower plot shows that the on-axis density of the  $H_2$  carrier gas even can exceed that of the  $D_2$  beam. A large amount of the carrier gas passes through the skimmer in contrast to the predictions. It seems that the mixing coefficients of hydrogen/deuterium are too high at these densities to create the carrier jet effect. The Monte Carlo simulations again verified the experimental results. It can be concluded that the Navier-Stokes equations, applied for the predictions [9] are not valid in the investigated flow range.

#### 4.4.2 Heavier gases

The mixing of two gases depends on their atomic or molecular diameters and masses. Thus an additional measurement was made using argon as inner and nitrogen as carrier gas. The dependences of the argon and nitrogen on-axis intensities on the nitrogen carrier-jet flow are found in Fig. 18. Here, contrary to the measurements with hydrogen and deuterium, the QMS-signal distributions are given without multiplication by the velocity, because the measured mean beam velocity  $v_x$  does not change in the studied range of  $Q_{N_2}$

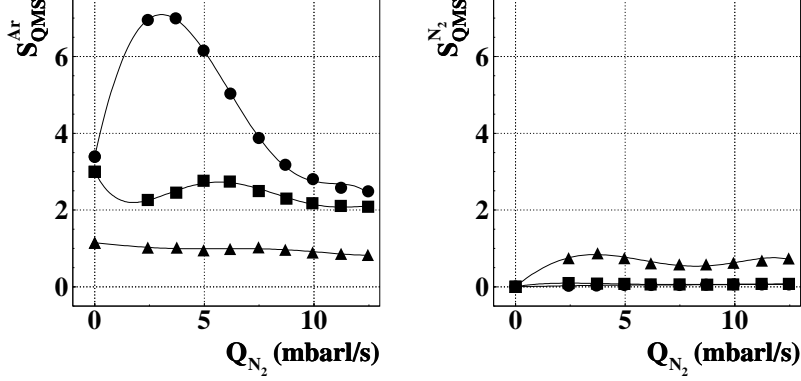


Fig. 18. The QMS signal of the inner argon gas (left) and the nitrogen carrier gas (right) as a function of the carrier gas flow  $Q_{\text{N}_2}$  for inner argon flows  $Q_{\text{Ar}} = 1$  mbarl/s (triangles), 4 mbarl/s (squares), and 7 mbarl/s (dots). The distance between skimmer-top and collimator was 35 mm and  $T_{\text{nozzle}} = 100$  K.

(see Fig. 19). The distributions of Fig. 18 are clearly different from those, measured with  $\text{D}_2$  as inner and  $\text{H}_2$  as carrier gas. For the highest argon flow of 7 mbarl/s, the measured on-axis argon intensity increases by a factor two from the argon expansion without carrier gas. Almost no nitrogen was detected in the QMS at argon flows higher than 3 mbarl/s.

The confirmation of the carrier-jet effect is found in the results of the TOF measurements. Fig. 19 shows the parameters of the beam with inner (argon) flow  $Q_{\text{Ar}} = 7$  mbarl/s as a function of the nitrogen-carrier flow  $Q_{\text{N}_2}$ . A clear cooling effect could be seen with a minimum around  $Q_{\text{N}_2} = 3$  mbarl/s, exactly where the intensity maximum appears (upper curve Fig. 18 left side). Thus the  $\text{N}_2$  beam cools the Ar beam without mixing because the mean velocity stays constant.

The density distribution calculated by the Monte Carlo simulation program of the argon expansion without (upper) and with carrier jet (middle) is shown

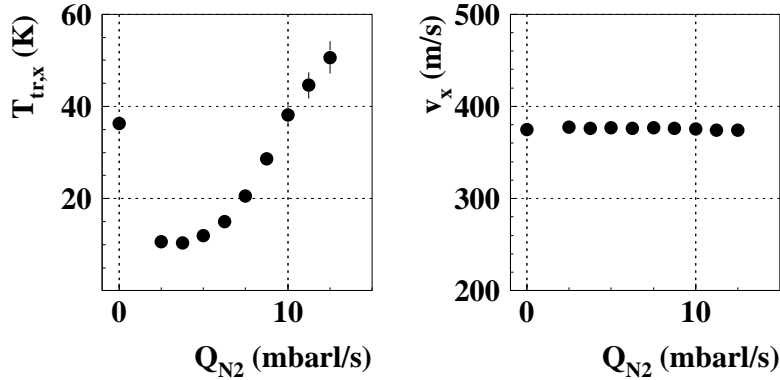


Fig. 19. Beam temperature  $T_{\text{tr},x}$  and mean velocity  $v_x$  of the inner argon gas as a function of the carrier gas flow rate  $Q_{\text{N}_2}$  for the inner argon flow of 7 mbarl/s (distance between skimmer top and collimator 35 mm,  $T_{\text{nozzle}} = 100$  K, cf. Fig. 18).

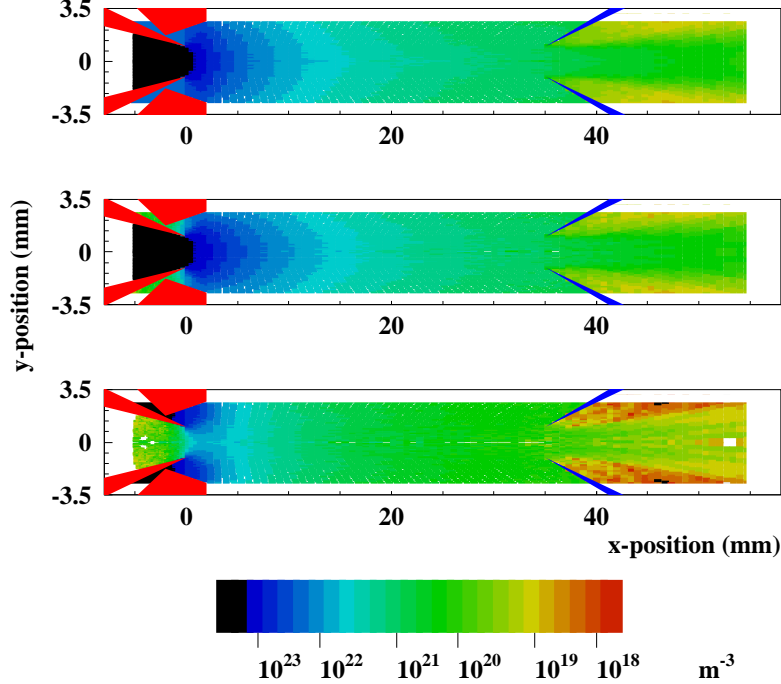


Fig. 20. Calculated distributions of the density in the expansion of an inner argon beam without carrier jet (upper plot) and the densities of the inner, argon, fraction (central plot) and the outer,  $N_2$ , fraction (lower plot) in the expansion with a carrier-jet. The gas flows were chosen as  $Q_{Ar} = 7 \text{ mbarl/s}$  and  $Q_{N_2} = 4 \text{ mbarl/s}$ .

in Fig. 20. The on-axis argon density is increased with the carrier gas flow rate  $Q_{N_2} = 4 \text{ mbarl/s}$  compared to the carrier-free expansion. The flow rate through the skimmer increases, while the divergence of the beam is almost the same. The on-axis density of the nitrogen carrier gas is very small as well as the flow through the skimmer in contrast to that of  $H_2$  Fig. 17. In both cases, the results of the DSMC calculations are consistent with those from the measurements. The mixing of the two gases is restricted to the boundary layer, and it obviously is much smaller than for hydrogen into deuterium in that flow regime. Therefore higher densities in the expansion would be required to reach a carrier-jet effect for deuterium/hydrogen. The degree of dissociation, however, for flow rates  $Q > 7 \text{ mbarl/s}$  is too low to achieve higher intensities by atomic beam sources.

## 5 A further application of the DSMC method

Apart from optimization of beam formation, the direct simulation Monte Carlo (DSMC) method can be applied to generate the input data for Monte Carlo simulations (see, e.g., Ref. [22]), where the atoms are tracked through the fields of the sextupole magnets in polarized atomic beam sources (ABS) as it has been mentioned in the introduction. Position and velocity distributions of the

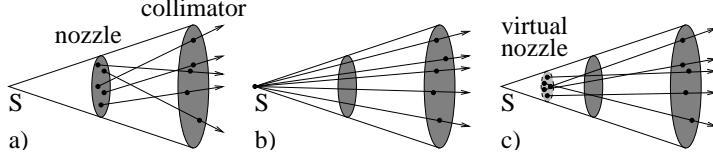


Fig. 21. Models used to define the input distribution of the atoms entering the sextupole system in tracking calculations (a: molecular flow model, b: laminar flow model, c: model of a flow in the transition region).

atoms on the collimator surface are needed as input data to achieve a correct calculation of the output intensity and polarization of the ABS. In addition to the velocity distributions in beam direction, determined by time-of-flight measurements like those of Ref. [23], a variety of models were used to create a sample of atoms passing the collimator [24].

- In the *molecular flow model* the connecting line between two randomly distributed points, one in the nozzle exit and the other in the aperture of the collimator, defines the direction of the atom (Fig. 21a).
- The *laminar flow model* uses the apex S of the cone, defined by the openings of nozzle and collimator, as the first point and a random point in the aperture of the collimator as the second one (Fig. 21b).
- The generalization is the *model of a flow in the transition region* (Fig. 21c). The first point is generated on a virtual nozzle and the second one is a random point in the aperture of the collimator. A molecularity parameter is defined as

$$K_{\text{mol}} = \frac{\log(1 - \frac{d_{\text{vn}}}{d_{\text{co}}})}{\log(1 - \frac{d_{\text{pn}}}{d_{\text{co}}})}, \quad (26)$$

where  $d_{\text{vn}}$ ,  $d_{\text{pn}}$  and  $d_{\text{co}}$  are the distances of the virtual nozzle, the physical nozzle and the collimator to the point S. For a given nozzle-collimator distance, the choice of  $K_{\text{mol}}$  defines the position of the virtual nozzle.

For the molecular flow model  $K_{\text{mol}} = 1$  and for the laminar flow model  $K_{\text{mol}} = 0$ . Furthermore,  $K_{\text{mol}} > 1$  means that the virtual nozzle lies between the real nozzle and the collimator. To decide, which of these models yields a satisfactory approximation of the real distributions of the particle directions and velocities, the model parameters can be compared with those resulting from DSMC calculations.

For the flow models, the unknown thermal non-axial velocity distributions can be approximated by a convolution of a function describing the nozzle-collimator geometry and a velocity distribution resulting from the measured mean axial velocity  $v_x$  and the axial beam temperature  $T_{\text{tr},x}$ ,

$$f(v'_j) = \int_{-v'_{j,\text{max}}}^{v'_{j,\text{max}}} \sqrt{1 - (v/v'_{j,\text{max}})^2} \exp\left(\frac{-m(v'_j - v)^2}{2k_{\text{B}}T_{\text{tr},x}c_j^2}\right) dv, \quad (27)$$



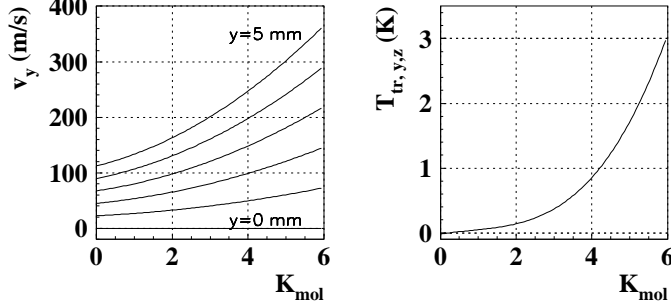


Fig. 22. Mean radial velocities of the hydrogen atoms in the collimator plane, calculated in the framework of the models of gas expansion for different distances  $y$  to the beam axis (left-hand side) and non-axial beam temperatures (right-hand side). The curves are given as function of the molecularity parameter  $K_{\text{mol}}$ .

where  $j = y$  and  $z$  denotes the components perpendicular to the beam direction in the coordinate system of Fig. 1. The parameter  $c_j$  is given by the nozzle-collimator geometry and the choice of the position of the virtual nozzle, i.e., the value of  $K_{\text{mol}}$ . Furthermore,  $v'_{j,\text{max}} = c_j \cdot v_x$  ( $j = y, z$ ) is the maximum transverse thermal velocity possible at the mean axial velocity  $v_x$  and  $c_j$ . The temperatures  $T_{\text{tr},j}$  of the gas with the use of eq. 12 are

$$T_{\text{tr},j} = \frac{m}{k_B} \cdot \overline{v_{\text{p},j}^2} = \frac{m}{k_B} \cdot \frac{\int_{-\infty}^{\infty} v_j'^2 f(v_j') dv_j'}{\int_{-\infty}^{\infty} f(v_j') dv_j'}. \quad (28)$$

The left-hand part of Fig. 22 shows the mean radial velocity of particles crossing the collimator aperture at different radial distances  $y$  from the beam axis. The right-hand part shows the non-axial beam-temperature dependence. The curves are given as a function of the molecularity parameter  $K_{\text{mol}}$ , which enters into the Eqns. 27 and 28 via the choice of  $c_j$ .

The parameters, obtained in the framework of the flow models, can be interpreted by comparison with those from DSMC calculations, presented in Fig. 23. By this comparison, the validity of the three models can be discussed concerning the distributions of the input data for the trajectory calculations.

- The molecular-flow model ( $K_{\text{mol}} = 1$ ) with the assumption of particle emission from the real nozzle allows  $T_{\text{tr},z}$  to be different from zero, because not all the trajectories lie within planes containing the beam axis. The non-axial temperatures  $T_{\text{tr},y}$  and  $T_{\text{tr},z}$ , resulting from the DSMC calculation with values around 2 K (Fig. 23), lie higher than the small values of  $\sim 0.1$  K from the model approximation. The DSMC calculation, however, may yield too high temperature values with the standard parameters in the code as it was discussed in section 4.1. Modification of the parameters might yield a lower temperature. The analysis of the density-distribution data, obtained with the DSMC code (Fig. 10) yields  $0 < K_{\text{mol}} < 1$ , which supports the

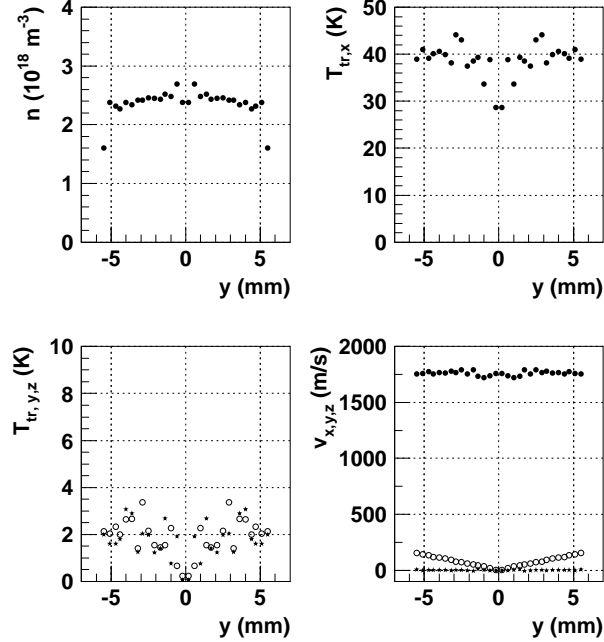


Fig. 23. Beam parameters of an expanding, partly dissociated hydrogen beam expansion calculated with the DSMC code (primary gas flow  $Q_{\text{H}_2} = 1 \text{ mbarl/s}$ , degree of dissociation  $\alpha = 0.8$ ,  $T_{\text{nozzle}} = 100 \text{ K}$ ,  $T_{\text{plasma}} = 3000 \text{ K}$ ). In the lower plots full circles denote the  $x$ , open circles the  $y$ , and stars the  $z$  direction.

applicability of this model. With emission of randomly distributed particles from the nozzle, it is the simplest model one can think of. It is thought to be applicable, when high accuracy is not requested in the tracking calculations.

- The laminar flow model ( $K_{\text{mol}} = 0$ ) was frequently used, since the radial beam profile, measured behind the collimator [22], was considered to be sufficiently consistent with that predicted by the model. Particle emission from a point like source on the beam axis implies that the non-axial beam temperatures are zero. The results of the DSMC calculations (Fig. 23), however, show that the transversal beam temperatures are different from zero (even, when they are reduced from the calculated  $T_{\text{tr},y,z} \approx 2 \text{ K}$  to  $1 \text{ K}$  due to the reasons given above for the molecular flow). A temperature of  $1 \text{ K}$  corresponds to a root mean square velocity of  $(\overline{v_{p,j}^2})^{1/2} = 91 \text{ m/s}$ . Total omission of those particle trajectories, not lying in planes containing the beam axis, means neglecting atoms with an angular velocity component and modified trajectories in the sextupole system due to the centrifugal force. Therefore, the laminar flow model is thought not to be suited to yield the appropriate input data.
- For the model of a flow in the transition region, the transversal beam temperatures from the DSMC calculation, reduced to  $1 \text{ K}$  as discussed above, according to Fig. 22 yield  $K_{\text{mol}} \sim 4$ . For this value, the increase of the transversal beam velocity  $v_y$  from the beam axis ( $y = 0$ ) to the aperture radius of the collimator ( $y = 5.5 \text{ mm}$ ) roughly match that of the DSMC data (Fig. 23). According to its definition, Eqn. 26, the virtual nozzle for

this value is positioned between the real nozzle and the collimator, which might be explained with particle emission from the freezing zone, i.e., the zone, where the laminar flow turns to the molecular flow.

The molecular-flow model and the model of a flow in the transition region are thought to be suited to yield the input-data distributions for the trajectory calculations in the sextupole magnets of a polarized ABS. The latter model might be the superior one, when the position of the virtual nozzle can be fixed to the appropriate position.

## 6 Summary and Conclusion

It has been shown that the direct simulation Monte Carlo (DSMC) method [7,13] is an excellent tool to describe the processes occurring in the expansion of light and also heavier gases in the transition region between laminar and molecular flow. The results of the calculations were confirmed by the measurements, performed at an atomic beam test stand (Fig. 4, [6]) with the use of an rf dissociator [5], a microwave [6] dissociator, and a novel atomic beam-profile monitor [8]. The origin of the discrepancies between simulated and measured temperatures was found, the problem could be solved [18,19] by modification of the appropriate input parameters of the DSMC code [13]. The predicted carrier-jet effect [9] could not be observed for hydrogen and deuterium at the operational parameters of atomic beam sources. It was, however, observed for an argon beam surrounded by a molecular nitrogen-carrier jet. Both experimental findings are consistent with the results of DSMC calculations. The problems, occurring with the so far used start generators for particle-trajectory calculations through the sextupole magnets of polarized atomic beam sources were studied. Uncertainties in the used models remain, and the distributions from DSMC calculations are considered to present the most reliable start generator.

## 7 Acknowledgments

We are grateful for the support provided by the DESY management and the DESY staff. In particular we acknowledge the help by the machine shops of MPI Heidelberg and the University Erlangen-Nürnberg. This work was supported by the German Bundesministerium für Bildung, Wissenschaft, Forschung und Technologie (BMBF 057ER12P(2), 06ER929I). Special thanks are due to N. Koch, A. Vassiliev, E. Hänisch, C. Bartels, V. Prahl, Y. Holler, K. Rith and the members of the HERMES experiment. Especially we want to thank M. Stancari for her studies of the effects by the choice of the input

parameters of the DSMC code. Finally we thank H. Seyfarth for the careful reading of the manuscript and fruitful suggestions.

## References

- [1] W. Haeberli, *Ann. Rev. Nucl. Sci* **17** (1967) 373.
- [2] S. Iannotta in: G. Scoles (Ed.), *Atomic and Molecular Beam Methods, Vol. I* (Oxford University Press, 1988) 683.
- [3] F. Stock et al., *Nucl. Instr. and Meth.* **A 343** (1994) 334.
- [4] A. Naß et al., *Nucl. Instr. and Meth.* **A 505** (2003) 633.
- [5] F. Stock et al., *Proc. Workshop on Polarized Beams and Polarized Gas Targets, Köln 1995*, H. Paetz gen. Schieck, L. Sydow (Eds.), (World Scientific, 1996) 260.
- [6] N. Koch and E. Steffens, *Rev. Sci. Instr.* **70** (1999) 1631.
- [7] G.A. Bird, *Molecular Gas Dynamics and the Direct Simulation of Gas Flows* (Clarendon Press Oxford, 1994).
- [8] A. Vassiliev et al., *Proc. Int. Workshop on Polarized Sources and Targets (PST99)*, Erlangen 1999, A. Gute, S. Lorenz, E. Steffens (Eds.), (Friedrich-Alexander-Universität Erlangen-Nürnberg) 200.
- [9] V.L. Varentsov et al., *Proc. 7<sup>th</sup> Int. Workshop on Polarized Gas Targets and Polarized Beams, Urbana 1997*, R.J. Holt, M.A. Miller (Eds.), *AIP Conf. Proc.* **421** (1997) 381.
- [10] A. Naß, PhD Thesis, Friedrich-Alexander-Universität Erlangen-Nürnberg (2002), <http://www-library.desy.de/diss02.html>.
- [11] D.R. Miller in: G. Scoles (Ed.), *Atomic and Molecular Beam Methods, Vol. I* (Oxford University Press, 1988) 14.
- [12] H. Haberland, U. Buck and E. Tolle, *Rev. Sci. Instr.* **56**, (1985) 1712.
- [13] G.A. Bird, computer code Ds2G, version 3.1.
- [14] A. von Engel, *Electric Plasmas: Their Nature and Uses*, (Taylor & Francis Ltd., London and New York, 1983).
- [15] W.S. Young, *Journal of Appl. Phys.* **46** (1975) 3888.
- [16] A. Winkler et al., *Appl. Phys.* **A67** (1998) 637.
- [17] American Institute of Physics Handbook (McGraw-Hill Inc., 2<sup>nd</sup> edition, 1963) 7-142.
- [18] M. Stancari, Internal Note INFN Ferrara **INFN/TC-06/11**, (2006) <http://www.lnf.infn.it/sis/preprint>.

- [19] M. Stancari, Proc. 12th Int. Workshop on Polarized Ion Sources, Targets and Polarimetry, Upton, NY 2007, AIP Conf. Proc. **980** (2008) 143.
- [20] M. Stancari, private communication (2008).
- [21] S.C. Brown, *Basic Data of Plasma Physics*, (AIP Press, American Institute of Physics, 1993).
- [22] W. Korsch, PhD Thesis, Phillips-Universität Marburg (1990).
- [23] B. Lorentz, Diploma Thesis, Ruprecht-Karls-Universität Heidelberg (1993).
- [24] B. Braun, PhD Thesis, Ludwig-Maximilians-Universität München (1995), <http://www-hermes.desy.de/notes/pub/95-LIB/braun.95.047e.thesis.ps.gz>.

## Appendix

The output parameters of the DSMC program [13] in the two output files of the first column are shown in the table below. The  $x$ - and  $y$ -coordinate refer to the center of the corresponding cell. The mean velocity of species  $i$  in  $j$ -direction is  $v_j^i = v_j - \Delta v_j^i$ . The overall temperature  $T$  is calculated as [7]

$$T = (3T_{\text{tr}} + \bar{\zeta}_{\text{rot}}T_{\text{int}}^{\text{rot}} + \bar{\zeta}_{\text{vib}}T_{\text{int}}^{\text{vib}})/(3 + \bar{\zeta}_{\text{rot}} + \bar{\zeta}_{\text{vib}}),$$

where  $\bar{\zeta}$  are the mean numbers of degrees of freedom of the species. It has to be mentioned that in the axially symmetric case utilized here,  $x$  is the beam direction,  $y$  the radial direction and  $z$  the circumferential direction, i.e.,  $v_z$  is tangential to the angular velocity.

output file	parameter	description	
ds2gf.txt	X COORD	$x$ coordinate	
	Y COORD	$y$ coordinate	
	(for the	DENSITY	mass density $\rho$
	entire	TR TEMP	kinetic temperature $T_{\text{tr}}$
	beam)	ROT TEMP	temp. of rotations $T_{\text{int}}^{\text{rot}}$
		VIB TEMP	temp. of vibrations $T_{\text{int}}^{\text{vib}}$
		OV TEMP	overall temperature $T$
		MACH	Mach number $M$
		U	} mean velocity $v_x, v_y, v_z$
		V	
	W	of all species	
ds2gm.txt	N DENS	number density $n$	
	TTX	kinetic temp. in x $T_{\text{tr},x}$	
	(for every	TTY	kinetic temp. in y $T_{\text{tr},y}$
	species)	TTZ	kinetic temp. in z $T_{\text{tr},z}$
		U DIF VEL	} mean velocity difference of a species $i$ in x, y, z $\Delta v_x^i, \Delta v_y^i, \Delta v_z^i$
		V DIF VEL	
		W DIF VEL	